NEUROSCIENCE

Tailoring of the axon initial segment shapes the conversion of synaptic inputs into spiking output in OFF-α T retinal ganglion cells

Paul Werginz[1,2]*, Vineeth Raghuram[1,3,4]*, Shelley I. Fried[1,3†]

Recently, mouse OFF-α transient (OFF-α T) retinal ganglion cells (RGCs) were shown to display a gradient of light responses as a function of position along the dorsal-ventral axis; response differences were correlated to differences in the level of excitatory presynaptic input. Here, we show that postsynaptic differences between cells also make a strong contribution to response differences. Cells in the dorsal retina had longer axon initial segments (AISs)—the greater number of $Na_v1.6$ channels in longer AISs directly mediates higher rates of spiking and helps avoid depolarization block that terminates spiking in ventral cells with shorter AISs. The pre- and postsynaptic specializations that shape the output of OFF-α T RGCs interact in different ways: In dorsal cells, strong inputs and the long AISs are both necessary to generate their strong, sustained spiking outputs, while in ventral cells, weak inputs or the short AISs are both sufficient to limit the spiking signal.

INTRODUCTION

At least 30 different types of retinal ganglion cells (RGCs) each extract different features of the visual world and use distinct patterns of spiking to convey information to downstream visual centers (1). The distinct patterns in each type are thought be shaped by different combinations of pre- and postsynaptic processing. For example, a given light stimulus results in unique patterns of presynaptic excitatory and inhibitory inputs for each RGC type. In addition, many different forms of postsynaptic processing have been identified in ganglion cells (2–4), including some that are unique to only specific types of ganglion cells; e.g., OFF-α, but not ON-α, ganglion cells of the mouse retina express a complement of ion channels that maintain spontaneous activity even in the absence of synaptic input (5). Little is known, however, about whether the pre- and postsynaptic mechanisms operating within RGCs are tuned to one another. For example, are the postsynaptic mechanisms within cells that receive strong, sustained excitatory synaptic input better suited to produce strong sustained spiking outputs than cell types that receive weaker and/or more transient inputs?

Spikes are initiated in the axon initial segment (AIS) of central nervous system (CNS) neurons, a specialized portion of the proximal axon that contains multiple types of densely packed voltage-gated sodium and potassium channels. Much recent work has shown that the AISs of individual types of neurons are customized so as to help to optimize specific aspects of neuronal function [reviewed in (6)]. For example, neurons of the nucleus laminaris (NL) that are sensitive to low auditory frequencies have AISs that are shorter and further from the soma than the AISs of neurons that are sensitive to high frequencies; the differences in the length and location of the AIS are thought to help maximize the sensitivity to interaural time differences for each frequency range (7). In addition, the AIS in

pyramidal cells of the somatosensory cortex helps to maintain a constant amplitude of somatic spikes across wide variations in cellular morphologies (8). Recent evidence indicates that AIS properties also vary systematically in RGCs, with both length and distance from the soma scaled to other neuronal features, e.g., ON-α sustained RGCs of the mouse with large dendritic fields have longer AISs that are also further from the soma (3). These variations are thought to help maintain response consistency across the population. Given the importance of the AIS in generating and shaping the spiking response of CNS neurons, we questioned here whether the AISs of individual RGC types were tailored, i.e., optimized to produce specific spiking patterns in RGCs as well. For example, are the AISs in cell types that generate sustained spiking responses different from the AISs in cell types that generate transient responses, and if so, what are the underlying design principles?

OFF-α transient (OFF-α T) RGCs of the mouse retina are an ideal cell type in which to study the role of the AIS and the interplay between postsynaptic processing (from the AIS) and presynaptic inputs. Recently, it was shown that the spiking responses in OFF-α T RGCs of the ventral portion of the mouse retina are more transient than those in the dorsal retina (9). The differences were shown to arise from differences in synaptic input, e.g., the excitatory input to dorsal cells is generally more prolonged than that to ventral cells. However, presynaptic differences do not preclude the possibility that postsynaptic differences also shape responses in these cells, and so here, we compare postsynaptic processing in cells of dorsal versus ventral retina. This approach will also allow us to correlate postsynaptic differences (e.g., AIS properties) to the presynaptic inputs delivered to each cell to gain insight into the factors that mediate postsynaptic processing. Use of a single cell type will help to minimize the anatomical and physiological differences between types and thus should help to better extract correlations.

Our goal was to investigate whether intrinsic postsynaptic differences in cells from different locations are complementary to the different presynaptic inputs received by each cell and, further, whether the two components act in tandem to help optimize neuronal responses. We started by injecting current into the somas to isolate the postsynaptic responses of individual cells. We found significant

[1]Department of Neurosurgery, Massachusetts General Hospital, Harvard Medical School, Boston, MA 02114, USA. [2]Institute for Analysis and Scientific Computing, Vienna University of Technology, 1040 Vienna, Austria. [3]Boston VA Healthcare System, Rehabilitation, Research and Development, Boston, MA 02130, USA. [4]Department of Biomedical Engineering, Tufts University, Medford, MA 02155, USA.
*These authors contributed equally to this work.
†Corresponding author. Email: fried.shelley@mgh.harvard.edu

differences between OFF-α T RGCs of the dorsal versus ventral retina and sought to understand how these differences arose. We started by comprehensively analyzing morphological properties, including the use of immunochemistry to obtain detailed anatomical measurements of the AIS from cells in both locations. We found systematic variation in AIS properties of OFF-α T RGCs with retinal location, i.e., the AIS properties of each cell are tuned to the level of presynaptic input it receives. Computational modeling was used to dissect the functional relationship between morphological properties and functional responses and revealed that AIS differences directly underlie response differences.

RESULTS

Intrinsic responses of OFF-α T RGCs vary with retinal location

Light responses of OFF-α T RGCs in the dorsal retina are more sustained than the responses of OFF-α T cells in the ventral retina (9). The differences in spiking are thought to arise from differences in the duration of the excitatory presynaptic input delivered to each location (input to dorsal cells is more prolonged than that to ventral cells). However, differences in the levels of presynaptic input do not preclude the possibility that intrinsic (postsynaptic) properties also contribute to the spiking differences, i.e., postsynaptic properties are different for dorsal and ventral OFF-α T RGCs and work in tandem with the presynaptic differences to produce the distinct spiking responses at each location. To explore this possibility, we used somatic current injections (see Materials and Methods) to isolate the intrinsic (postsynaptic) responses of individual OFF-α T RGCS (Fig. 1A, left) and compared responses between cells at dorsal versus ventral locations (Fig. 1A, right). OFF-α T RGCs were tentatively identified by their large somas and characteristic responses to stationary light flashes (fig. S1) (5, 9, 10); confirmation of cell type was made from the stratification level of terminal dendrites, obtained through immunochemical processing and confocal microscopy after completion of electrophysiological experiments (see Materials and Methods and fig. S1).

Injections of small depolarizing currents (e.g., +100 pA) led to increased spiking in both ventral and dorsal cells (Fig. 1B, top row). Small increases in the amplitude of the stimulus pulse led to increases in the rate of firing. Further increases, however, led to several characteristic changes in the firing pattern. For example, in ventral cells, the amplitude of elicited spikes gradually decreased, and spiking was eventually interrupted by periods of silence (e.g., Fig. 1B, left, red arrow). As the amplitude continued to increase, a more pronounced loss of consistency was observed in the spiking pattern, i.e., spike amplitude decreased faster and the duration of the periods without spiking became longer. An analogous disruption of spiking was observed for OFF-α T RGCs located in the dorsal retina but occurred at higher amplitudes than the cells in the ventral retina (Fig. 1B, right). We use the term "failure threshold" to indicate the stimulus amplitude at which spiking began to break down, i.e., the number of elicited action potentials was less than that elicited by the next lowest amplitude (the red and blue horizontal arrows in Fig. 1B indicate the failure thresholds for the ventral and dorsal cells, respectively). Failure thresholds were significantly lower for cells in the ventral retina than for cells in the dorsal retina (495 ± 29 pA versus 718 ± 40 pA, $P = 2 \times 10^{-4}$; Fig. 1C).

To further characterize the intrinsic response differences between ventral and dorsal cells, we examined firing rate versus time for cells at each location (Fig. 1D, same two cells as in Fig. 1B). Responses to current injection were separated into an initial phase (100 ms), followed by a weaker and more sustained second phase that persisted for the duration of the stimulus; we use the terms transient and sustained phases to denote these portions of the response (0 to 100 ms and 100 to 400 ms, respectively). The rate of firing was always highest within the transient phase and increased monotonically with increasing levels of current injections. In contrast, the firing rate during the sustained phase increased with increasing levels of depolarizing currents for low amplitudes but then decreased as the amplitude of the current injection increased further (consistent with the results of Fig. 1B). To compare the firing rates across the population of ventral and dorsal cells, we performed two sets of measurements. The first was to compare the response of all cells to a 300-pA current injection; this level was chosen because it produced relatively strong responses without exceeding the failure threshold in almost all cells (two ventral cells had a failure threshold of 300 pA and were excluded from this analysis). At this level of current injection, peak firing rate (192 ± 4 Hz versus 214 ± 5 Hz, $P = 0.0026$), sustained firing rate (65 ± 3 Hz versus 102 ± 7 Hz, $P = 1 \times 10^{-5}$), and sustained-to-peak ratio (inset: 0.34 ± 0.01 versus 0.47 ± 0.03, $P = 0.0001$) were all significantly higher in dorsal cells (Fig. 1E). The second comparison was similar but used the stimulus amplitude that generated the highest numbers of spikes in each cell, i.e., the stimulation level was optimized independently for each cell. Once again, peak firing rate (233 ± 14 Hz versus 323 ± 16 Hz, $P = 0.0001$), sustained firing rate (166 ± 10 Hz versus 75 ± 7 Hz, $P = 4 \times 10^{-8}$), and sustained-to-peak ratio (inset: 0.32 ± 0.02 versus 0.52 ± 0.02, $P = 3 \times 10^{-8}$) were all significantly higher in dorsal cells (Fig. 1F). In both comparisons, the use of amplitudes below the failure threshold helped to ensure that the observed response differences between the two populations were not simply due to the breakdown of spiking at lower amplitudes in ventral cells. In addition to spike rate, the total number of spikes elicited in response to a given stimulus was also higher in dorsal cells, especially for stronger amplitudes (Fig. 1G, left). Most of this difference arose during the sustained phase (Fig. 1G, right) as there was little difference between ventral and dorsal cells during the transient phase (Fig. 1G, middle). Together, these results suggest three intrinsic differences between OFF-α T RGCs of the dorsal versus ventral retina: (i) Dorsal cells are responsive to a wider range of stimulus amplitudes, (ii) dorsal cells are capable of generating higher rates of spiking than ventral cells and generate higher rates of spiking to a given stimulus, and (iii) dorsal cells generate higher spike counts to a given stimulus. Thus, in addition to the differences in the presynaptic input arriving at dorsal versus ventral cells (9), there are also intrinsic differences in how synaptic input is converted into spike trains for cells at each location. The remainder of this study explores the anatomical and biophysical factors that contribute to these response differences.

Dorsal and ventral OFF-α T RGCs have distinct morphological features

We reasoned that differences in the responses to current injection are likely to arise from differences in morphological structure and/or intrinsic biophysical properties between cells at the two locations and started our analysis by comparing passive membrane properties between dorsal and ventral OFF-α T RGCs. We focused initially on the possibility that input impedance differences were contributing
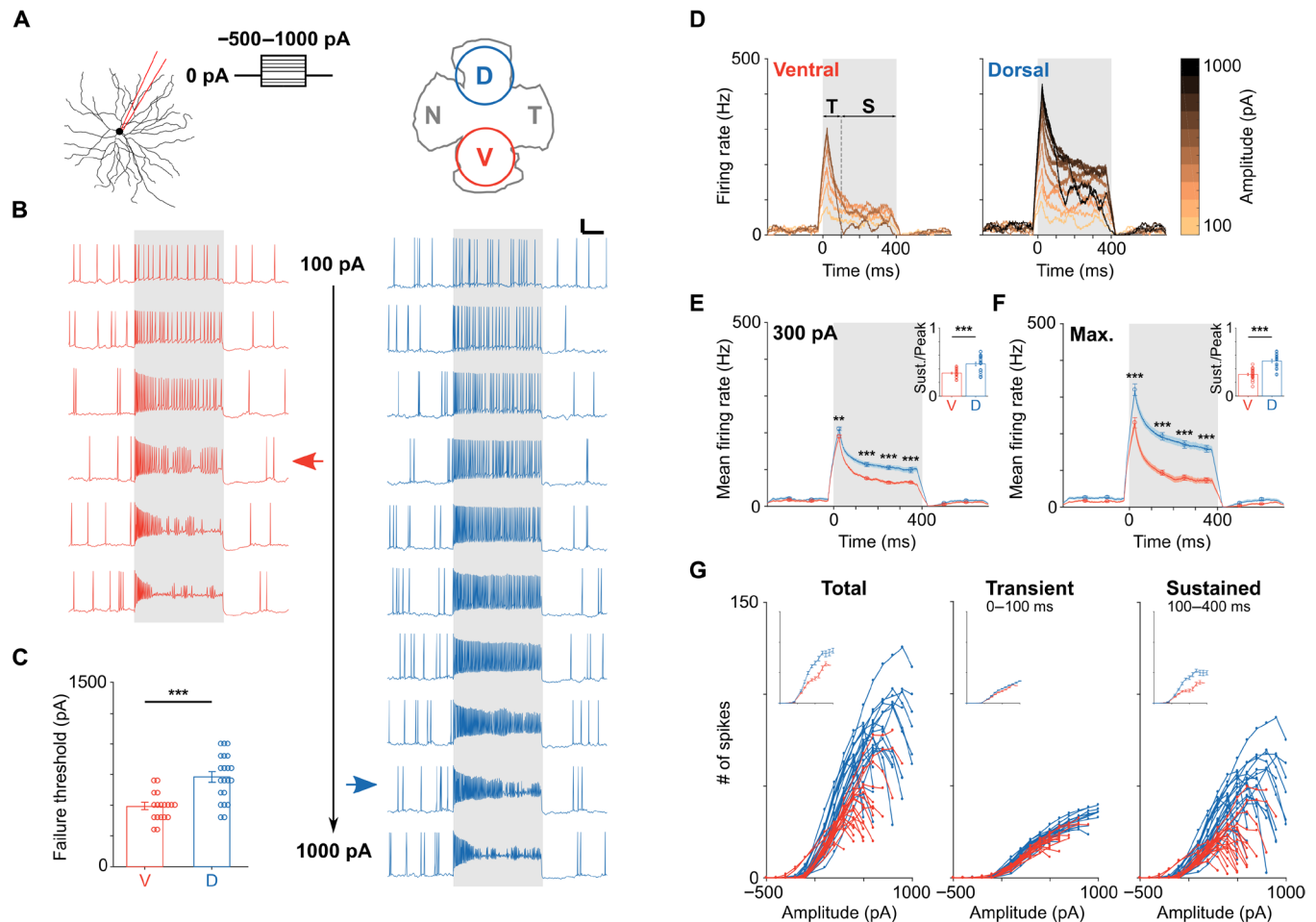
Fig. 1. Spiking responses are weaker in ventral versus dorsal OFF-α T RGCs. (**A**) Left: Whole-cell patch clamp recordings were used to record the responses of OFF-α T RGCs to current injections (range, −500 to 1000 pA). Right: Schematic of the whole mount mouse retina depicting the approximate sampling locations for ventral (V) and dorsal (D) cells. (**B**) Representative current clamp recordings from OFF-α T RGCs in the ventral (red) and dorsal (blue) retina. Pulse duration was 400 ms (gray shading), amplitudes ranged from 100 to 600 pA (ventral) and 100 to 1000 pA (dorsal), respectively. Scale bar, 100 ms/20 mV. Horizontal arrows indicate failure threshold (see main text). (**C**) Comparison of failure threshold between ventral (red, $n = 20$) and dorsal (blue, $n = 22$) cells (495 ± 29 pA versus 718 ± 40 pA, $P = 2 \times 10^{-4}$). (**D**) Plots of firing rate versus time for all stimulus amplitudes tested; same cells as (B). Transient (T) and sustained (S) response phases correspond to 0 to 100 ms and 100 to 400 ms, respectively. (**E**) Mean firing rate over time across the population of ventral (red) and dorsal (blue) cells in response to a stimulus amplitude of 300 pA [two-way repeated measures analysis of variance (ANOVA): interaction, $P = 0.0002$; subgroups, $P = 9 \times 10^{-6}$]. (**F**) Same analysis as in (E) but for the amplitude that elicited maximum responses in each cell (two-way repeated measures ANOVA: interaction, $P = 4 \times 10^{-6}$; subgroups, $P = 3 \times 10^{-8}$). Insets in (E) and (F) show the ratio of sustained and peak firing rate for ventral (red) and dorsal (blue) cells. (**G**) The number of elicited spikes is plotted versus injected current amplitude for ventral (red) and dorsal (blue) cells for the whole duration of the injection (left), the initial 100 ms (middle), and the last 300 ms (right) of the stimulus. Insets show the population mean. **$P < 0.01$; ***$P < 0.001$.

to the differences in failure threshold and adapted the current injection experiments of Fig. 1 to compare impedances between dorsal and ventral cells (fig. S2). Hyperpolarizing current injections (range, −100 to −500 pA) were injected into the soma of individual cells, and the corresponding change in membrane voltage was determined and used to calculate input resistance (fig. S2). There was no significant difference between the two populations (44.2 ± 0.4 megohm versus 43.0 ± 0.5 megohm, $P = 0.6487$). We also compared action potential kinetics and resting membrane voltage, again, finding no significant differences between ventral and dorsal cells (fig. S3).

We next compared the anatomical properties of dorsal versus ventral cells, focusing on the neuronal elements known to influence spiking, e.g., the soma, dendrites, the proximal axon, and the AIS, the portion of the proximal axon in which spikes are initiated. Warwick *et al.* (*9*) reported a small difference between the diameters of

the dendritic fields in dorsal versus ventral cells but no difference in the diameter of their somas. We confirmed both of these findings (soma diameters: 18.0 ± 0.4 μm versus 18.5 ± 0.4 μm, $P = 0.4018$; fig. S4; dendritic field diameters: 280 ± 7 μm versus 347 ± 8 μm, $P = 3 \times 10^{-7}$; Fig. 2A). The difference in dendritic sizes found here is slightly larger than that reported by Warwick *et al.* (*9*)—the discrepancy is almost certainly due to our avoidance of cells close the midline (where the dendritic field size differences are smallest) (see Materials and Methods). In addition to dendritic field size, we also compared several other aspects of the underlying dendritic structure including total dendritic length, mean segment length, and dendritic branching (fig. S4). Both total dendritic length and mean segment length were found to scale linearly with dendritic field diameter, and the effects were similar for both dorsal and ventral cells. Sholl analysis revealed that dendritic branching patterns were also similar across both populations.
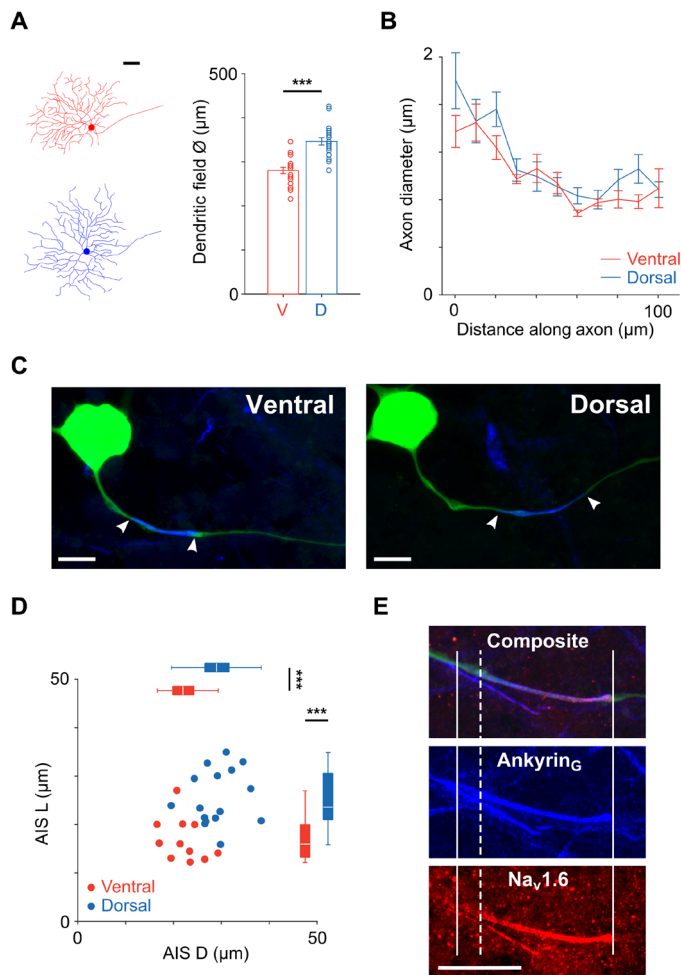
Fig. 2. AIS properties are different in ventral and dorsal OFF-α T RGCs. (A) Left: Tracings of representative ventral (red; dendritic field diameter ~290 μm) and dorsal (blue; dendritic field diameter ~370 μm) cells. Scale bar, 50 μm. Right: Comparison of dendritic field diameter between ventral (red; $n = 21$) and dorsal (blue; $n = 20$) cells (280 ± 7 μm versus 347 ± 8 μm, $P = 3 \times 10^{-7}$). **(B)** Axon diameter was traced along the first 100 μm of the proximal axon in ventral (red; $n = 13$) and dorsal (blue; $n = 17$) cells (two-way repeated measures ANOVA: interaction, $P = 0.8101$; subgroups, $P = 0.2336$). **(C)** Confocal images of the soma and AIS from typical ventral (left) and dorsal (right) OFF-α T RGCs. Staining for Ankyrin$_G$ (blue) is overlaid with the axon (green); the start and end of the AIS are indicated by white arrowheads. Scale bars, 20 μm. **(D)** Scatter plot of AIS length (AIS L) versus AIS distance (AIS D) for ventral (red; $n = 11$) and dorsal (blue; $n = 16$) cells. Box plots reveal statistically significant differences for both distance (22.3 ± 1.2 μm versus 29.2 ± 1.2 μm, $P = 0.0004$) and length (16.9 ± 1.4 μm versus 25.5 ± 1.4 μm, $P = 0.0003$). **(E)** Immunochemical staining for Ankyrin$_G$ (blue) and Na$_v$1.6 (red) along the proximal axon. Solid vertical lines indicate the start and end of the Ankyrin$_G$ staining; the dashed vertical line indicates the start of the Na$_v$1.6 portion. Scale bar, 20 μm. ***$P < 0.001$.

Thus, although the field sizes are different for the two populations, the underlying dendritic structures were similar.

The shape of the proximal portion of the axon has been shown to influence the initiation of spikes in the AIS and the effectiveness with which the axonal spike triggers the somatic spike (11, 12) and therefore could also be contributing to the response differences found here. We therefore compared the morphology of proximal axons in dorsal and ventral OFF-α T RGCs. For each cell, we measured the axon diameter at its junction with the soma and then again at 10 μm steps for distances up to 100 μm from the soma (Fig. 2B). For both ventral and dorsal cells, the diameter gradually decreased along the first 60 to 80 μm of the proximal axon to a diameter of ~0.8 μm after which it widened slightly (to ~1 μm) and remained uniform (11). There were no significant differences between cells from the two locations, suggesting that the response differences do not arise from size differences of the proximal axon itself.

The AIS is a specialized portion of the proximal axon in which action potentials are initiated (13); densely packed voltage-gated sodium channels within the AIS underlie its high sensitivity to depolarization and help to trigger the spike (14). Outside the retina, much previous work has shown that differences in the length or the location of the AIS can influence different elements of neuronal function (7, 8, 14, 15), and therefore, we considered the possibility that the AIS might function differently in dorsal versus ventral cells. As a first step in this evaluation, we determined the properties of the AIS (length and location) for cells from each location.

Similar to previous studies that have characterized the AIS, both in the retina (3, 16, 17) and in other types of CNS neurons (8, 18), we immunochemically stained for Ankyrin$_G$, a structural protein that anchors sodium channels at a high density within the AIS and nodes of Ranvier (see Materials and Methods) (19). Figure 2C shows the soma and proximal axon (green) from a typical ventral (left) and a typical dorsal (right) OFF-α T RGC, along with an overlay of the region stained for Ankyrin$_G$ (blue). Because Ankyrin$_G$ staining has previously been shown to accurately capture the full extent of the AIS (16, 20), the region of overlapping staining between the axon and Ankyrin$_G$ was used as a marker for the length of the AIS (AIS L) (white arrowheads in Fig. 2C indicate the start and end of the AIS). AIS distance (AIS D) was defined as the distance between the soma and the proximal edge of the AIS. Plotting length versus distance for all cells in which AIS measurements were made (Fig. 2D) revealed a significant difference between ventral and dorsal cells with ventral cells having AISs that were both shorter (16.9 ± 1.4 μm versus 25.5 ± 1.4 μm, $P = 0.0003$) and closer to the soma (22.3 ± 1.2 μm versus 29.2 ± 1.2 μm, $P = 0.0004$) than the AISs of dorsal cells. Both length and distance of the AIS were correlated to cell size (fig. S5) (3).

Na$_v$1.6 channels of the AIS are thought to support the generation of high-frequency firing in CNS neurons (21–23). For example, the rate of sustained firing is substantially lowered in medTg Scn8a (sodium channel, voltage gated, type VIII, α)-null RGCs lacking Na$_v$1.6 channels (23). We therefore questioned whether the Na$_v$1.6 component of the AIS would itself be different for cells in the two locations, given the stronger spiking in dorsal cells. To evaluate this, we stained a subset of ventral and dorsal cells with an antibody specific for the Na$_v$1.6 subtype (Fig. 2E). The Na$_v$1.6 component was found to occupy the majority of the AIS in both populations (Fig. 2E and fig. S6) but was longer in dorsal cells. The ratio of Na$_v$1.6 length to total AIS length was generally similar across both populations (fig. S6). The maintenance of a consistent ratio is analogous to the situation in α sustained RGCs (3), although the ratio there was closer to 90%. We did not investigate why different ratios are found in these two cell types, and it will be interesting to learn the functional role of this ratio, as well as whether the ratios are consistent in other RGC types as well.

Together, the anatomy measurements reveal two principal differences between dorsal and ventral OFF-α T RGCs. First, the dendritic fields of dorsal cells are larger than those of ventral cells.

Second, the AISs of dorsal cells are larger and also further from the soma than the AISs of ventral cells. We next ran a series of electrophysiology experiments and computer simulations to investigate whether and how these anatomical differences contribute to the physiological response differences between the two populations.

The AIS mediates the response differences between dorsal and ventral cells

Through trial and error, we found that gentle but persistent scraping across the proximal axon with the tip of the patch pipette (see Materials and Methods) could be used to sever the axon (Fig. 3A) and thus detach the AIS (and distal axon) from the rest of the neuron, e.g., the soma and dendritic compartments. The ability to remove portions of the axon was intriguing because it allowed us to gain insight as to the role of the AIS by comparing responses to current injection in intact cells to responses in cells where the AIS had been removed. Although we could not precisely control the exact location at which the cut was made, axotomy locations were reliably limited to within ~125 μm of the soma (range, 0.5 to 126.2 μm); the actual location of each cut was not determined until after completion of physiological measurements and used the same immunochemical methods described earlier (see Materials and Methods). In a subset of cells ($n = 5$), the axotomy process damaged the cell, resulting in strong increases to the rate of spontaneous firing, and markedly altered spike kinetics; cell death occurred rapidly in these cells. In the remaining cells ($n = 15$), axotomy did not adversely affect the health of the cells as overall cell function in axotomized cells remained similar to that of nonaxotomized cells (fig. S7).

In 6 of the 15 cells that were axotomized, the cut occurred between the soma and the AIS, i.e., the portion of the axon containing the AIS was no longer connected to the cell (representative cells are shown in the two rightmost panels of Fig. 3A). We repeated the current injection experiments of Fig. 1 in these cells and found a slight reduction in both the strength and duration of the response for ventral cells (Fig. 3B, red traces) but a much more substantial reduction for dorsal cells (Fig. 3B, blue traces); the sustained portion in particular was strongly reduced. As a result of the disproportionate reductions, responses to current injection became largely similar in all cells missing an AIS. Failure thresholds also became similar for both dorsal and ventral cells (Fig. 3C, 425 ± 25 pA versus 450 ± 50 pA, $P = 0.6328$). Failure thresholds in axotomized ventral cells were only slightly lower than those for intact cells (425 ± 25 pA versus 495 ± 29 pA, $P = 0.2908$), but in dorsal cells, the difference was more substantial (450 ± 50 pA versus 718 ± 40 pA, $P = 0.0729$). We also compared firing rate over time for axotomized cells and found no significant difference between the two groups (Fig. 3D). Overlay of firing rate versus time for intact ventral cells (black trace) highlights the similarity in function with axotomized cells.

In the remaining axotomized cells ($n = 9/15$), the cut occurred beyond the region of dense Ankyrin_G staining, i.e., the AIS remained intact and functionally connected to the soma. In these cells, responses to current injection remained largely similar to those from nonaxotomized cells (fig. S7). Thus, the axotomy experiments suggest that the AIS helps to enhance the neuronal responses, especially the sustained component of dorsal cells, while the shorter and more proximal AISs of ventral cells have a much smaller influence on spiking responses. Further, because removal of the axon distal to the AIS had little effect on response, our results suggest that the AIS alone is sufficient to enhance the response.
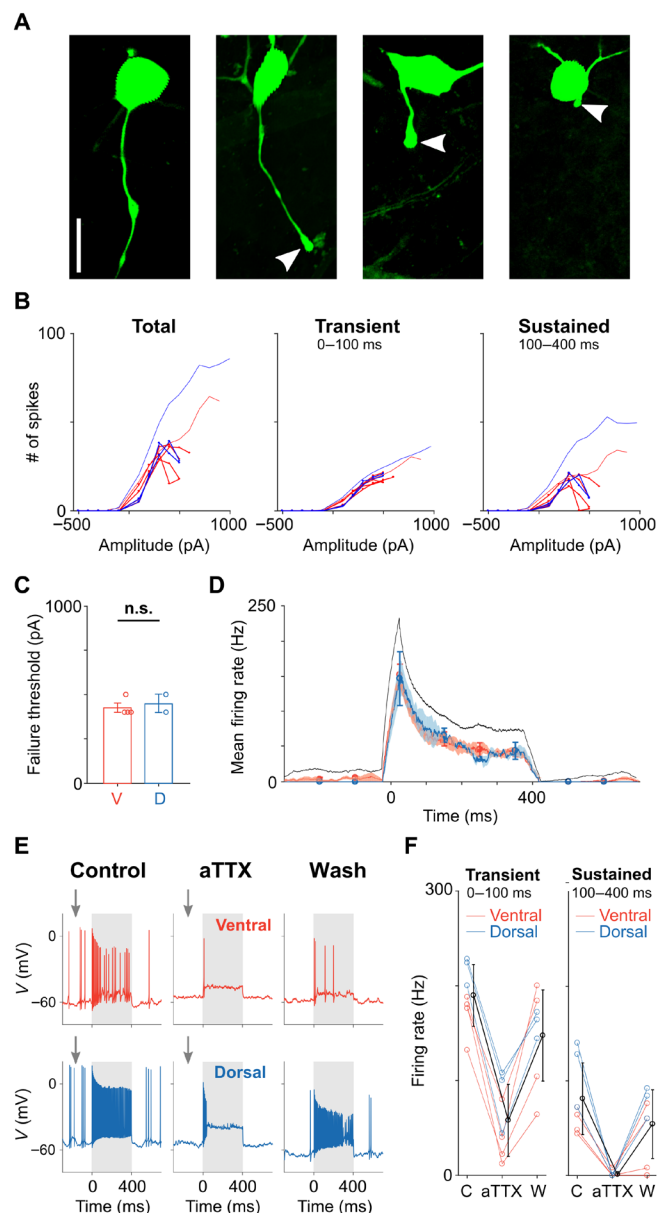

Fig. 3. Sustained firing is altered by disruption of AIS function. (**A**) Confocal images of one cell with an intact axon (left) and three axotomized cells in the three rightmost panels. The severed edge of each axon is indicated by an arrowhead. Scale bar, 20 μm. (**B**) Number of spikes elicited for current injections in ventral (red; $n = 4$) and dorsal (blue; $n = 2$) cells that had their axons removed between the soma and the AIS. Three time periods were examined: (i) the full duration of the stimulus (left), (ii) the initial 100 ms (middle), and (iii) the final 300 ms of the stimulus (right). Population means of intact cells are shown by thin lines. (**C**) Comparison of failure thresholds between ventral (red; $n = 4$) and dorsal (blue; $n = 2$) cells that had axotomies between the soma and the AIS (425 ± 25 pA versus 450 ± 50 pA, $P = 0.6328$). n.s., not significant. (**D**) Mean firing rate over time across the population of axotomized ventral (red; $n = 4$), intact ventral (black; data from Fig. 1F), and dorsal (blue; $n = 2$) cells in response to a stimulus amplitude that elicited maximum responses in each cell. (**E**) Recordings before (left), during (middle), and after (right) the addition of aTTX (4,9-anhydrotetrodotoxin) (500 nM) to the perfusion bath for a ventral (red; top) and dorsal (blue; bottom) cell. (**F**) Comparison of peak/transient (left) and sustained (right) components of the response under control (C), during the application of aTTX, and after wash (W) in ventral (red; $n = 4$) and dorsal (blue; $n = 3$) OFF-α T RGCs. Population means are shown in black. Error bars represent one SD.

As can be inferred from the two distributions of axotomy sites (0.25 to 25.9 μm and 62.2 to 126.2 μm), the location of the cut was never within the AIS itself. We did not investigate why this was the case, but it seems likely that one or more structural proteins that support the dense packing of voltage-gated sodium channels, e.g., Ankyrin$_G$, add structural stability to this portion of the axon, and thus preferentially shift the axotomy location to a proximal or distal location.

The experimental manipulation that required to successfully perform the axotomy was challenging, and we were only able to complete the experiment in a small number of cells. However, because the AISs of these cells are composed primarily of Na$_v$1.6 channels, we could reversibly "eliminate" the AISs using aTTX (4,9-anhydrotetrodotoxin), a selective and highly potent blocker of Na$_v$1.6 channels (24, 25), thereby allowing us to confirm our findings from the axotomy experiments. Similar to the axotomy experiments, the addition of aTTX to the perfusion bath led to complete elimination of the sustained phase of the responses to current injection (Fig. 3E). Substantial but incomplete recovery of responses was observed after aTTX was washed out (Fig. 3F and fig. S6). Similarly, the sustained phase of the response to light was also eliminated when aTTX was applied (the transient phase was reduced) (fig. S6). In addition, the robust spontaneous spiking observed in both dorsal and ventral cells under control conditions was greatly reduced in the presence of aTTX (Fig. 3E, arrows). Given the consistent results from both physical and chemical elimination of the AIS, we conclude that the location-dependent response differences between ventral and dorsal OFF-α T RGCs are largely mediated by the AIS differences, especially by the Na$_v$1.6 channels within the AIS.

Longer AISs are associated with stronger depolarization and more robust spiking

The injection of current caused a shift in the baseline somatodendritic membrane voltage in all cells (Fig. 4A, green); we refer to this shift as ΔV. Plotting the number of spikes as a function of ΔV allowed us to compare spike generating capabilities across cells at common levels of membrane depolarization (Fig. 4B; all measurements from a given cell are connected by a line; blue, dorsal cells; red, ventral cells). Response patterns were quite different for cells from the dorsal versus ventral retina (Fig. 4B). Dorsal cells generated a larger number of spikes for a given level of ΔV, especially for ΔV levels greater than ~10 mV; most of the difference occurred during the sustained portion of the response (Fig. 4B, right). The range of ΔV values resulting from current injection was largely similar for the two populations. Note, however, that for a given level of ΔV, dorsal cells generated a larger number of spikes than ventral cells. The difference was most apparent in the sustained component of the response, consistent with the results of Fig. 1B, which suggested that cells from both locations can generate a response that is initially robust but that dorsal cells are better able to maintain sustainedness over the course of the response, especially at more depolarized levels of somatic membrane voltage. Note also that while the range of ΔV values appeared to be slightly wider for dorsal cells, this was only because we stopped testing the response to current injection in each cell once spiking levels became significantly reduced, i.e., the larger ΔV values in dorsal cells are plotted because these cells continued to function at higher levels of ΔV than ventral cells. We determined the level of ΔV in each cell at failure threshold (ΔV_{fail}) and found substantially higher levels in dorsal cells (15.5 ± 0.8 mV versus
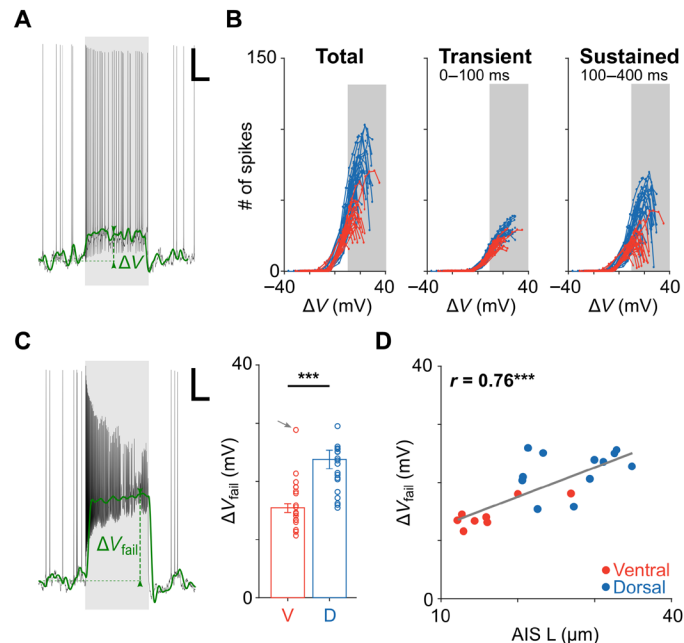

Fig. 4. Longer AISs facilitate higher levels of depolarization. (**A**) Responses to current injection consisted of a series of action potentials "riding" on top of a change in the baseline membrane voltage (green); the change in V (from resting) is referred to as ΔV. Scale bar, 100 ms/10 mV. (**B**) Plots of the number of elicited spikes as a function of ΔV in ventral (red; $n = 17$) and dorsal (blue; $n = 20$) cells elicited during the full extent of the stimulus (left), during the initial response phase (middle), and during the sustained response phase (right). Gray shading indicates $\Delta V > 10$ mV. (**C**) Left: ΔV_{fail} was defined as the change in V at failure threshold. Scale bar, 100 ms/10 mV. Right: ΔV_{fail} was significantly lower in ventral (red; $n = 17$) versus dorsal (blue; $n = 20$) cells (15.5 ± 0.8 mV versus 23.8 ± 1.6 mV, $P = 4 \times 10^{-5}$). One ventral cell was considered an outlier and excluded from analysis (gray arrow). (**D**) Each circle is a plot of ΔV_{fail} versus AIS length for an individual ventral (red; $n = 8$) or dorsal (blue; $n = 12$) RGC. The gray line is the best-fit linear regression ($P = 0.0001$). ***$P < 0.001$.

23.8 ± 1.6 mV, $P = 4 \times 10^{-5}$; Fig. 4C). Thus, the spike generators of dorsal cells continue to function effectively at more depolarized levels of membrane voltage, while the spike generators of ventral cells become less effective at these same levels. It is likely that the increased effectiveness in dorsal cells arises from their longer AISs as there was a strong positive correlation between ΔV_{fail} and the length of the AIS (Fig. 4D).

Na$_v$1.6 channel properties underlie faster spike rates in dorsal cells

Besides remaining more effective at stronger levels of depolarization, dorsal cells were also found to generate higher rates of spiking for a given stimulus (Fig. 1), and so, we explored whether AIS properties also affect the strength of the spiking response. We reasoned that differences in AIS properties might result in differences in the thresholds for somatic spike initiation and/or differences in the waveform of the somatic spike itself (AIS-initiated spikes trigger somatic spikes), both of which could influence the number of spikes arising in response to current injection. To explore this, we compared the spike waveforms from cells with different size AISs and focused initially on cells with long AISs versus cells missing the entire AIS (axotomized cells with the cut between the soma and the AIS). Figure 5A shows an overlay of spikes from several axotomized cells and reveals considerable variability in kinetics. Cells in which
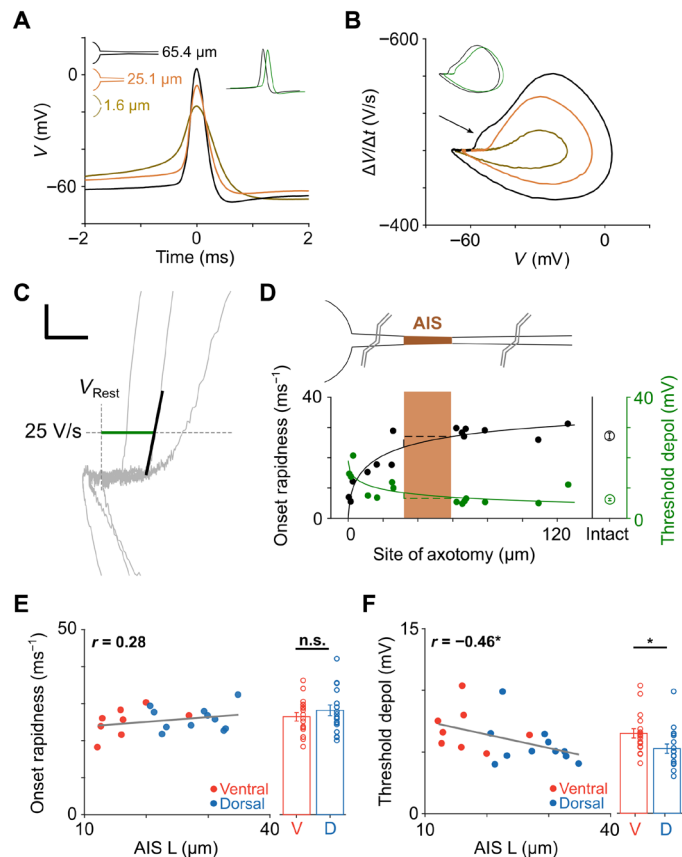
Fig. 5. Spike dynamics are altered by removal of the AIS. (**A**) Overlay of spontaneous spikes from three axotomized cells (different distances from the soma for each). The inset shows a comparison of the spike with the longest axon segment remaining with a spike from an intact cell (green); an arbitrary horizontal offset was used to enhance visibility of the two traces. (**B**) Overlay of phase plots for the same spikes on the left. The arrow indicates the initial segment-somatodendritic break in the cell with the longest axonal segment. The inset shows a comparison of the same spike with a spike from an intact cell (green); an arbitrary horizontal offset was again used to enhance visibility of the two traces. (**C**) Two parameters were extracted from phase plots: (i) threshold depolarization (green) and (ii) onset rapidness (black) (see main text). Scale bar, 10 mV/20 V/s. (**D**) Threshold depolarization (green) and onset rapidness (black) are plotted versus the location of the axotomy ($n = 16$). Solid lines are best-fit Hill functions, and dashed lines indicate potential other transitions of onset rapidness and threshold depolarization. Average values from cells with intact axons are shown at right. Schematic on top and shaded box indicate the approximate location of the AIS (brown); points to the left of the shading indicate axotomies between the soma and the AIS, whereas points right to the shading indicate axotomies beyond the AIS. (**E**) Scatter plot of AIS length versus onset rapidness ($P = 0.2454$) and comparison of onset rapidness between ventral (red; $n = 18$) and dorsal (blue; $n = 18$) cells (26.4 ± 1.1 ms^{-1} versus 28.1 ± 1.4 ms^{-1}, $P = 0.3981$). (**F**) Scatter plot of AIS length versus threshold depolarization ($P = 0.0484$) and comparison of threshold depolarization between ventral (red; $n = 18$) and dorsal (blue; $n = 18$) cells (6.5 ± 0.4 mV versus 5.2 ± 0.4 mV, $P = 0.0119$).

the axon was missing had very slow kinetics, while cells with relatively long axon segments (axotomy was furthest from the soma) exhibited the fastest kinetics; these differences did not arise from a change in the cell's input impedance after axotomy as impedance levels were similar for axotomized and intact cells (fig. S2). Spike kinetics in cells with a distal axotomy were highly similar to those

from intact cells (Fig. 5A, inset). Phase plots, i.e., plots of $\Delta V/\Delta t$ versus V, allow the kinetics of the action potential to be compared in finer detail and better highlighted the differences between the same three spikes. In particular, the phase plots revealed higher levels of peak depolarization and higher rates of membrane depolarization for cells with longer axonal segments (Fig. 5B). Note again the same similarity in kinetics between intact cells and those with a distal axotomy (inset).

To quantify the differences across the full population of axotomized cells, we calculated the initial rate of membrane depolarization, referred to as onset rapidness (26), by determining the slope of the phase plot when $\Delta V/\Delta t$ first exceeds 25 V/s (Fig. 5C, black line). Plots of onset rapidness as a function of axotomy location are shown in Fig. 5D (black) and confirm that cells with short or no remaining axons had the slowest initial depolarization. The plots also confirm that there was no significant difference in onset rapidness between cells with intact axons and cells in which the axon was severed beyond the AIS (26.2 ± 1.7 ms^{-1} versus 27.1 ± 1.0 ms^{-1}, $P = 0.6657$). Similar to the effect of axotomy, onset rapidness was strongly decreased in intact cells when Na$_v$1.6 channels were blocked with aTTX (fig. S6). On the basis of these results, we questioned whether the larger AISs of intact dorsal cells might result in higher onset rapidness values versus those of (intact) ventral cells; the difference was fairly small (26.4 ± 1.1 ms^{-1} versus 28.1 ± 1.4 ms^{-1}, $P = 0.3981$; Fig. 5E) (see Discussion).

Threshold depolarization was defined as the deviation from resting potential at which the level of $\Delta V/\Delta t$ reaches 25 V/s, i.e., the level of membrane depolarization at which the spike is induced (Fig. 5C, green horizontal line) (26). Casual observation of the phase plots for the axotomized cells of Fig. 5B reveals that spike onset occurs at relatively hyperpolarized levels in cells with an intact AIS and a relatively depolarized level in the cell with the entire axon removed. Similar results were found across the population of axotomized cells in that the longest axons were associated with the lowest thresholds (Fig. 5D, green). Consistent with the onset rapidness results, threshold depolarization was similar for cells with an axotomy beyond the AIS and cells that were intact (6.3 ± 0.6 mV versus 6.2 ± 0.4 mV, $P = 0.8619$). Unlike the comparisons of onset rapidness between intact dorsal and ventral cells, however, we found significantly lower threshold depolarizations in intact dorsal cells versus intact ventral cells (6.5 ± 0.4 mV versus 5.2 ± 0.4 mV, $P = 0.0119$; Fig. 5F). The results therefore suggest that longer AISs enhance the efficacy of the spike initiation process by shifting the threshold for (somatic) spike initiation to more hyperpolarized levels. As expected, blockage of Na$_v$1.6 channels (using aTTX) strongly shifted thresholds to more depolarized levels (fig. S6), suggesting that the observed effects are largely mediated through Na$_v$1.6 channels.

To gain further insight into the relationship between AIS length, spike threshold and the rate of spiking, we built a series of computational models (see Materials and Methods) that allowed us to systematically test the effects of specific anatomical features on physiological responses. We started by comparing the responses in a single-compartment model composed of either Na$_v$1.1 or Na$_v$1.6 channels (Fig. 6, A to C). Different activation thresholds in Na$_v$1.1 versus Na$_v$1.6 channels were implemented in the model through the Hodgkin-Huxley kinetics driving the behavior of each sodium channel subtype (see Materials and Methods). Overlay of phase plots of the individual spikes arising from each of the two sodium
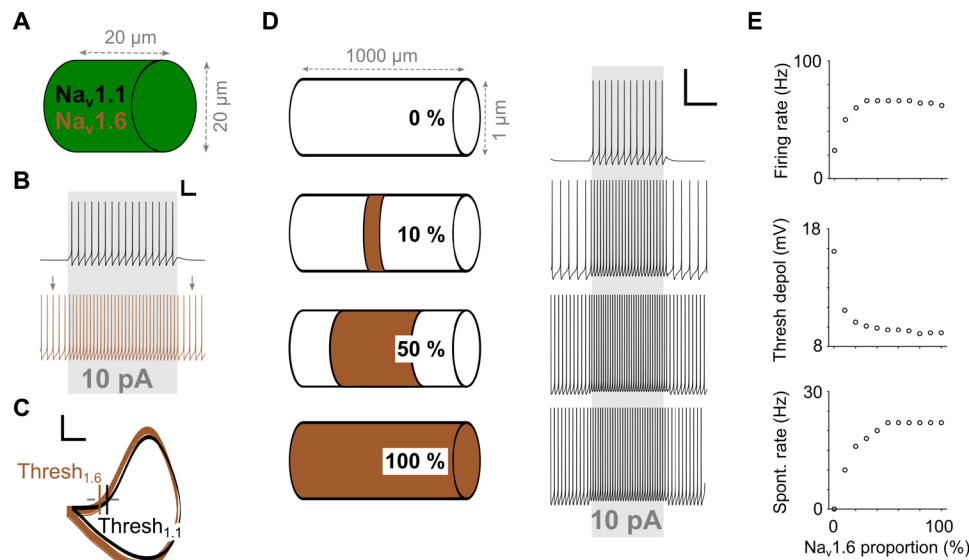
Fig. 6. Simple models of AIS-specific spiking properties. (**A**) A cylindrical single-compartment model was equipped with either $Na_v1.1$ or $Na_v1.6$ channels. (**B**) Firing rate in response to a current injection of 10 pA was higher when $Na_v1.6$ channels were inserted into the model. Gray arrows indicate spontaneous spiking. Scale bar, 50 ms/20 mV. (**C**) Phase plots derived from (B) reveal a lower threshold for the $Na_v1.6$ model than for the $Na_v1.1$ model. Scale bar, 20 mV/200 V/s. (**D**) Left: A 1-mm axon model was created with 201 compartments. All compartments were uniform except each had only $Na_v1.6$ channels or only $Na_v1.1$ channels; the percentage of compartments with $Na_v1.6$ channels increased from 0 (top) to 100% (bottom) across different simulation trials; $Na_v1.6$ channels were always centered around the middle compartment. Right: Spiking response to a 10-pA current injection into the center compartment for the four configurations on the left. Scale bar, 200 ms/20 mV. (**E**) Firing rate (top), threshold depolarization (middle), and spontaneous firing rate (bottom) at the center compartment as a function of the $Na_v1.6$ portion within the axon.

channel subtypes reveals the lower onset threshold (more hyperpolarized) for $Na_v1.6$ channels (Fig. 6C) as expected. We next ran simulations with a multicompartment axon model in which all compartments were anatomically and biophysically identical except for the type of sodium channel in each compartment ($Na_v1.6$ or $Na_v1.1$). To simulate the increase in AIS length, we systematically increased the number of compartments with $Na_v1.6$ channels (Fig. 6D) and found that the introduction of $Na_v1.6$ into even a small number of compartments resulted in a substantial decrease in threshold depolarization and an increase in firing rate and spontaneous firing rate (Fig. 6E). Further increases in the number of compartments that contained $Na_v1.6$ channels, i.e., larger AISs, resulted in even lower thresholds but the magnitude of the effect diminished and eventually leveled off as AIS length continued to increase.

We expanded the model into a morphologically and biophysically realistic OFF-α T model cell (see Materials and Methods) and repeated the current injection experiments. Preliminary results with this model revealed that key elements of natural neuronal function were replicated, e.g., spikes were initiated in the AIS, the AIS spike triggered the somatic spike, and the kinetics of individual action potentials closely matched that of actual OFF-α T RGCs (fig. S8). There was also good agreement with the current injection experiments of Fig. 1 (fig. S8). Once the baseline performance of the model was established, the length of the AIS was systematically varied across the range of sizes found immunochemically (10 to 35 μm) and the response to current injection determined for each length. Consistent with the results from the simpler models and the physiological experiments, longer AISs led to the initiation of somatic action potentials at more hyperpolarized levels of membrane voltage. For example, comparison of the action potentials elicited from a 10-μm-long AIS versus a 35-μm-long AIS (representing ven-

tral and dorsal cells, respectively) revealed a more hyperpolarized threshold in the longer (dorsal) model cell (Fig. 7A). As suggested from the traces in Fig. 7A, increasing the length of the AIS in this model also leads to faster rates of spiking (Fig. 7B, unfilled circles). Analysis of our physiological data confirmed the correlations between AIS length and firing rates: The firing rate of both the sustained and transient components of the responses increased with increasing AIS length (Fig. 7C). To confirm that the influence of AIS length was not dependent on a specific location of the AIS (i.e., a fixed distance between the AIS and the soma), we ran an additional set of simulations in which the AIS was shifted toward or away from the soma (Fig. 7B, filled points); changes in AIS location (AIS D variations) did not substantially influence the firing rate for a given AIS length. As expected from their slower onsets, firing rates also decreased with increasing levels of threshold depolarization (Fig. 7D). This occurred in both model cells (Fig. 7D, unfilled circles) and in physiological experiments (Fig. 7D, red and blue points). Thus, the presence of a greater number of high-sensitivity $Na_v1.6$ channels within longer AISs resulted in lower activation thresholds and, correspondingly, higher rates of AIS spiking in both model cells and physiological experiments, confirming a direct correlation between the anatomical differences of the AIS and physiological responses to current injection.

To evaluate whether the AIS differences between dorsal and ventral cells also influence the responses to light (not only the strong, rectangular current injections used in Fig. 1), we injected the excitatory synaptic input currents that arise in response to light stimuli into morphologically and biophysically realistic model cells (Fig. 7E). To isolate the influence of the synaptic input in these simulations, we blocked all active ionic currents in the model cell and tuned the input resistance of each model cell (fig. S2) to precisely match
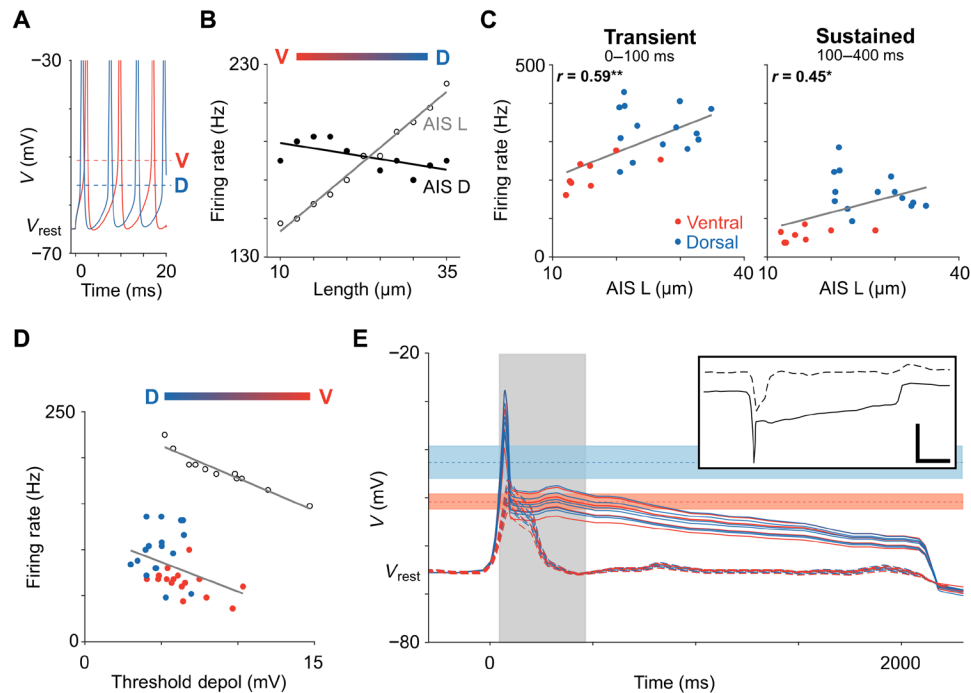
Fig. 7. Realistic models of AIS-specific spiking properties. (**A**) Overlay of simulated spikes from the realistic model cell with short (10 μm; red) and long (35 μm; blue) AISs. Dashed horizontal lines indicate thresholds for spike initiation. (**B**) The influence of AIS L (unfilled circles) and AIS D (filled circles) on sustained firing rate in response to a somatic current injection of 300 pA. (**C**) Scatter plots of AIS length versus transient (left; $P = 0.0036$) and sustained firing rates (right; $P = 0.0347$) from physiological experiments. The stimulus amplitude used was the one that resulted in the strongest responses in each cell. Solid lines in indicate best-fit linear regressions. *$P < 0.05$; **$P < 0.01$. (**D**) Firing rate in response to a 300-pA stimulus is plotted as a function of threshold depolarization for recorded data (red and blue correspond to ventral and dorsal cells, respectively) and simulated spike trains [black; data from (B)]. (**E**) Inset shows the input currents elicited during light stimulation in a typical ventral (dashed) and dorsal (solid) cell as measured by (9). Scale bar, 250 ms/500 pA. These currents were injected into the somas of model RGCs and the membrane voltage over time was plotted in ventral (red; $n = 6$) and dorsal (blue; $n = 6$) cells (main) with all voltage sensitive ion channels blocked. Red and blue horizontal shadings indicate failure threshold ± one SD as measured in ventral and dorsal RGCs, respectively. Gray shading indicates the 400-ms time window that was used in the current clamp experiments of Fig. 1.

experimental data. Because the increased AIS length in dorsal cells appears to shift the level at which depolarization block occurs to more depolarized levels, we were particularly interested in the effects of physiologically realistic synaptic inputs on membrane voltage. The light-elicited synaptic input arising in a dorsal OFF-α T RGC is shown in Fig. 7E [inset, adapted from (9)] and generated a brief, strong depolarization peak (~50-ms duration) that reduced and plateaued to a level of ~10 to 20 mV more depolarized than the resting membrane voltage (Fig. 7E, overlaid solid lines); responses were highly similar across all dorsal (blue) and ventral (red) model cells. The red horizontal band in Fig. 7E corresponds to the level of membrane depolarization (ΔV) that caused depolarization block in ventral cells (Fig. 4C)—because the plateau depolarization levels are largely within this band, the results suggest that sustained synaptic input would trigger depolarization block in cells with short AISs (i.e., ventral cells). That is, if dorsal cells did not have long AISs, then the synaptic input they receive in response to sustained light stimuli would lead to depolarization block, and spiking would be truncated. The blue horizontal band corresponds to the higher ΔV levels at which depolarization block occurred in dorsal cells; the fact that the plateau from light responses is below this level is consistent with the finding of sustained spiking in dorsal cells (9). The excitatory synaptic input arising from light stimuli to ventral cells was much more transient (Fig. 7E, inset, dashed line), and the resulting membrane depolarization was more transient as well (Fig. 7E,

dashed line). The brevity of these inputs greatly reduces the potential for depolarization block, and thus, AIS length is much less critical in these cells (see Discussion).

DISCUSSION

Building upon previously described differences in the strength and duration of the presynaptic inputs to ventral versus dorsal OFF-α T RGCs (9), we observed here that there were also differences in the intrinsic processing performed by cells at the two locations. The AIS in dorsal cells was longer and more distally located; this arrangement facilitated the creation of the stronger and more sustained bursts of spiking that arise in these cells. In contrast, the shorter and more proximal AISs in ventral cells limited the strength and duration of their spike bursts. Thus, both pre- and postsynaptic specializations shape the output of OFF-α T RGCs but interact in different ways: In dorsal cells, strong inputs and the long AIS are both necessary to generate their strong, sustained spiking outputs, while in ventral cells, weak inputs or the short AIS is both sufficient to limit the spiking signal. The specificity of the individual configurations suggests that the postsynaptic properties of OFF-α T RGCs are tailored to their presynaptic inputs, an arrangement that helps to ensure that the appropriate responses are reliably generated at each location and possibly enhance the evolutionary benefit (9) associated with the different responses at each location.

Longer AISs underlie the stronger responses in dorsal cells

The intrinsic responses of OFF-α T RGCs were isolated by injecting depolarizing current into the somas of individual RGCs and revealed significant differences between cells located in dorsal versus ventral retina: Dorsal cells generated higher frequencies of spiking for a given level of input current and also remained responsive over a wider range of stimulus amplitudes (Fig. 1). Severing the axon between the soma and AIS greatly reduced the strength and the duration of responses in cells at both locations (Fig. 3), indicating that the proximal axon plays an important role in shaping the response to current injection. When the axon cut occurred distal to the AIS (i.e., the connection between the AIS and the somatodendritic region was left intact), responses to current injection were highly similar to those from intact cells (fig. S7), suggesting that the AIS, but not more distal portions of the proximal axon (27), plays the key role in shaping the responses of these cells. Further, because responses at the two locations were similar when the AIS was removed but different with the AIS intact, the axotomy experiments also strongly suggested that the AISs were functionally different in cells from the two locations. Consistent with this, immunochemical staining revealed that the AISs were longer and more distant from the soma in dorsal cells (Fig. 2). When we compared anatomical and physiological results in individual cells, we found that longer AISs were strongly correlated to lower thresholds for spike initiation (Fig. 5F) and to higher peak firing rates (Figs. 1 and 7D). Simulations in a series of models, ranging from a simple, one-compartment model to an array of morphologically and biophysically realistic multicompartment models, revealed that the lower thresholds can arise directly from the wider extent of $Na_v1.6$ channels and their lower thresholds for activation. The lower thresholds led to faster onsets of spiking with a corresponding increase in firing rates (Fig. 7D). Thus, our results suggest that increases to the length of the AIS not only lower the threshold for eliciting single action potentials (28) but also underlie the generation of higher firing rates. Our modeling results suggest that the distance between the AIS and the soma had only a limited role in generating the stronger responses (Fig. 7B). Similar to results from Lazarov et al. (26), our model also predicts larger onset rapidness with increasing AIS length; however, we did not observe these differences in recordings. It is possible that nature uses additional mechanisms between the soma and AIS to ensure constant onset rapidness (i.e., reliable infiltration of AIS spikes into the somatodendritic compartments) (15) that were not part of our model. Variations in AIS D from the soma might also be important for the normalization of somatic action potentials as reported by a previous study (8).

Our finding here that longer AISs lower the activation threshold for single spikes and enhance the duration and spike count in response to the injection of current is consistent with the findings from analogous experiments in hippocampal dentate gyrus cells (DGCs) (28). In DGCs, repetitive activation over a 3-hour period led to the reduction of the length of the AIS, which resulted in higher thresholds for the activation of single spikes and a reduction in the length and strength of elicited spike trains. While the parallels are noteworthy, it is likely that there are substantial differences between the spike generating mechanisms of DGCs and RGCs. For example, the highest spike counts in DGCs typically remained below 10, while the lowest spike counts in OFF-α T RGCs ranged from 30 to 40 and went as high as 100. Spiking rates were also much higher in RGCs. Somewhat paradoxically, the length of the AIS is

shorter in ventral OFF-α T RGCs (16.9 ± 1.4 μm) than that reported in DGCs (19.2 ± 0.7 μm), suggesting that while AIS length imparts stronger responses within a single cell type, many additional factors may contribute to each cell's overall level of response. While we did not investigate the factors that underlie the large response differences between OFF-α T RGCs and DGCs, there are several likely contributions including predominately $Na_v1.2$ channels in DGCs versus predominately $Na_v1.6$ channels in RGCs (with faster kinetics and higher sensitivity). The more distal location of the AIS relative to the soma (in RGCs) is also likely to further reduce activation threshold.

The variation of AIS properties across the dorsal-ventral axis of OFF-α T RGCs is somewhat analogous to the variation in AIS properties reported across the caudolateral-ventromedial axis within the NL of the chick auditory system (7). In the NL, high characteristic frequency (CF) neurons at the rostromedial end have AISs that are shorter and more distal from the soma, while low CF neurons at the caudolateral end have AISs that are relatively long and close to the soma; the differences help to optimize sensitivity to the specific CF processed by each neuron. Thus, although the range of AIS lengths in the two systems was similar, variations in AIS properties are used differently by each, e.g., they help ensure an appropriate duration of the spike train in RGCs, while in NL neurons, they optimize sensitivity to different frequencies of sound. They play a third role in L5 pyramidal neurons of somatosensory cortex (8) (maintaining a consistent amplitude of the somatic spike across a wide range of cell sizes); the different functions raise questions about whether there are even more roles to be found and/or the AIS performs multiple roles in some cell types. Consistent with this possibility, firing rate during the transient phase of the response was somewhat correlated to AIS length (Fig. 7C, left), but the y intercept of the plot was quite high (~200 Hz), suggesting that the AIS may only have a limited influence on transient responses. This notion is strongly supported by our axotomy (Fig. 3, A to D) and pharmacology experiments (Fig. 3, E and F), in which transient responses persisted, albeit slightly weaker, when the AIS was eliminated. Given that ventral cells only generate transient responses, this suggests the possibility that the AIS plays some other role. The y intercept was much closer to zero for the sustained firing rate (Fig. 7C, right), consistent with the notion that AIS length plays a critical role in maintaining sustained spiking, especially in dorsal cells. Other elements of the AIS (besides length and location) are likely to contribute to shaping spiking patterns. For example, we found here that the overlap of $Na_v1.6$ channels and Ankyrin$_G$ is constant within a given cell type of the retina (fig. S6), but different for other cell types (3), suggesting that this ratio may have a functional role as well. In addition, specific types of voltage-gated ion channels may be expressed in the AISs of some cell types but not others and thus impart additional differences between types.

Do Na$_v$1.6 channels mediate the expanded dynamic range of dorsal cells?

The breakdown of action potential generation at high levels of depolarization is referred to as depolarization block and has been reported previously in retinal and other types of CNS neurons (29–31). Modeling results from these studies suggest that the block arises from insufficient deinactivation of sodium channels during the repetitive firing caused by prolonged depolarization (29). This is consistent with our finding that cells with longer AISs, which have

a corresponding increase in the number of available channels, enter depolarization block at higher levels of depolarization than cells with shorter AISs do (Fig. 4D). Cells with longer AISs also had larger dendritic fields; however, input resistance was similar in ventral versus dorsal cells (fig. S2). This suggests that the longer AISs in dorsal cells contribute additionally to their ability to maintain robust spike generation at higher levels of depolarization. The $Na_v1.6$ channels that comprise the bulk of the AIS (Fig. 2E) exhibit rapid recovery from inactivation (32) and can generate resurgent (21, 22) and persistent currents (32), all of which would support maintained firing at higher levels of depolarization [reviewed in (33)]. Pharmacologically blocking $Na_v1.6$ currents with aTTX resulted in a marked decrease in the cell's ability to generate high-frequency spiking, both in response to intracellular current injections (Fig. 3E) and to light stimulation (fig. S6), suggesting that $Na_v1.6$ channels are an essential contributor to spike generation in these cells, i.e., the increased number of $Na_v1.6$ channels help to preserve spike function at increased levels of depolarization. The contribution of $Na_v1.6$ channels to the maintenance of high rates of spiking is consistent with much previous work in other CNS neurons (21, 22, 32). Other factors may also contribute to the expanded dynamic range observed here in cells with longer AISs. For example, $K_v1.2$ channels are expressed at the same locations as $Na_v1.6$ channels in rat RGCs (17), and therefore, dorsal OFF-α T RGCs may also have more channels available to help repolarize the AIS membrane, with a corresponding reduction in the potential for insufficient deinactivation.

MATERIALS AND METHODS
Electrophysiology
The care and use of animals followed all federal and institutional guidelines and all protocols were approved by the Institutional Animal Care and Use Committee of the Massachusetts General Hospital. Before anesthesia, animals were dark-adapted for approximately 30 min. All procedures following anesthesia were conducted under dim red light to avoid bleaching of photoreceptors. Adult (postnatal days 35 to 120) wild-type mice (C57BL/6J, the Jackson laboratories) were anesthetized with isoflurane (Henry Schein) and subsequently euthanized by cervical dislocation. Eyeballs were harvested, and retinas were dissected from the eyecup and mounted, photoreceptor side down, onto a recording chamber. The retina was subsequently perfused with oxygenated Ames medium buffered to pH 7.4 (Sigma-Aldrich) at a flow rate of 2 to 3 ml/min for the duration of the experiment. Temperature was maintained at ~34°C. Small holes were made in the inner limiting membrane to obtain access to RGC somas. Spiking responses were obtained using whole-cell patch recordings. Intracellular solution consisted of 125 mM K-gluconate, 10 mM KCl, 10 mM Hepes, 10 mM EGTA, 4 mM Mg–adenosine 5′-triphosphate, and 1 mM Na–guanosine 5′-triphosphate (all Sigma-Aldrich). Morphological analysis was allowed by adding NEUROBIOTIN (0.25 mM; Vector Laboratories) and Alexa Fluor 488 (0.5%; Invitrogen) to the intracellular solution. After break-in, the pipette series resistance was compensated with the bridge balance circuit of the amplifier (<15 megohm). Recorded membrane voltage was corrected for the change in liquid junction potential (−8 mV) (34). A third-order Butterworth filter (cutoff frequency, 20 Hz) was used to extract membrane polarization (ΔV) excluding action potentials. We reasoned that we could compare the spike generating capabilities across cells by depolarizing them to the same level (same ΔV) and

then comparing the resulting spiking patterns. Although we could not determine a priori the ΔV that would result in a given cell from a given set of stimulus conditions, we injected a range of stimulus amplitudes into each cell and thus generated responses for a range of ΔV levels in each cell. This allowed us to plot the number of spikes elicited as a function of ΔV for each cell and then compare results across cells at common ΔV levels.

Light stimuli were used only to help distinguish OFF-α T cells from other types of RGCs, especially from OFF-α sustained RGCs and other types of α cells (with large somas and brisk firing). We have found a 300-μm flashed (bright) spot to be particularly useful in this regard. Light responses are only used for a tentative identification as final confirmation of cell type incorporates comparison of dendritic field size, morphology, and stratification level of the terminal dendrites, to the well-described norms for this cell type (see below). We did not calibrate light levels, but the background intensity was fairly bright, and we estimate it to be about ~4 nW/m^2. Flashed spots were 300 μm in diameter, 1000 ms in duration, and 60% contrast. OFF-α T cells were targeted by their large somas (diameter, >14 μm) and identified by their characteristic light responses (5, 9, 10). To enhance the likelihood of detecting differences, we avoided cells close to the midline of the dorsal-ventral axis (where differences might be subtle) and, instead, targeted cells closer to the dorsal and ventral edges. Because of the narrower spatial extent over which cells were targeted, we did not attempt to identify the relative location of each cell along the dorsal-ventral axis and, instead, limited classification to either "dorsal" or "ventral" (Fig. 1A, right).

aTTX (500 nM; Tocris Bioscience) was used to block $Na_v1.6$ channels. Recordings after wash out of aTTX were performed within 15- to 25-min onset of wash.

Stimulus control and data acquisition were performed with custom software written in LabVIEW (National Instruments) and MATLAB (MathWorks). Data were recorded using an Axopatch 700B amplifier (Molecular Devices) and digitized by a data acquisition card (PCI-MIO-16E-4, National Instruments). The timing of individual spikes was detected as the depolarization (positive) peak of each spike in the raw trace. Firing rate was computed by pooling responses from multiple trials (≥3) and subsequent convolution with a 50-ms sliding window.

Immunohistochemistry
Retinal whole mounts with fills of OFF-α T RGCs were fixed in 4% paraformaldehyde (w/v) solution for 30 min, washed in phosphate-buffered saline (PBS) (pH 7.4) for 1 hour, and subsequently placed into 12-well clear multiwell plates (Corning Falcon) for processing through free-floating immunochemistry. Retinas were then blocked with 5% normal donkey serum (NDS) in 0.3% PBTX (10× PBS + Triton X-100) solution for 2 hours and then incubated with Alexa Fluor 488–conjugated streptavidin (1:200; Invitrogen), mouse anti-Ankyrin$_G$ (1:200; NeuroMab), rabbit anti-$Na_v1.6$ (1:200; MilliporeSigma), and goat anti–choline acetyl-transferase (ChAT) (1:200; MilliporeSigma) in 1% NDS with 0.3% PBTX solution for five overnights. Following incubation in primaries, samples were washed in PBS for 2 hours (4× for 30 min) and placed in Alexa Fluor 488–conjugated streptavidin (1:200; Invitrogen), Cy5-conjugated donkey anti-mouse (1:200; Jackson ImmunoResearch), Alexa Fluor 405–conjugated donkey anti-rabbit (1:200; Abcam), and Alexa Fluor 594–conjugated donkey anti-goat (1:200; Invitrogen) secondary antibodies in 0.3% PBTX solution for one overnight. Last, samples were washed in PBS for 1 hour (2× for

30 min), mounted with ProLong Gold antifade mounting medium (Invitrogen), coverslipped, and placed in 4°C refrigeration until further confocal imaging.

Image acquisition and analysis
Fluorescence imaging was performed with a laser scanning confocal microscope (ZEISS LSM 880 with Airyscan) using Zeiss Efficient Navigation (ZEN Pro) software to acquire and export images. Images of the full RGC dendritic field morphology were acquired with ×20 magnification at a $x/y/z$ resolution of 0.15 μm by 0.15 μm by 0.31 μm, while images of the soma and proximal axon with AIS labeling were acquired with a 63× oil immersion objective (numerical aperture, 1.4) at a $x/y/z$ resolution of 0.09 μm by 0.09 μm by 0.31 μm. The use of a higher magnification (×63) allowed for the ability to perform precise tracing around the cell body and dendritic tree structures. Anatomical measurements and image after processing of confocal scans were performed in National Institutes of Health (NIH) ImageJ/Fiji package (35).

Confirmation of cell type was obtained using ChAT, an immunochemical marker that labels the processes of ON and OFF starburst amacrine cells. These are, otherwise, referred to as (ON- and OFF-) ChAT bands and can be used to delineate the specific sublamina in which the terminal dendrites of tentatively identified RGCs stratified (1, 10). Consistent with previous reports, the terminal dendrites of putative OFF-α T RGCs stratified between the ON- and OFF-ChAT bands.

The anatomical properties (e.g., start and end position, distance from the soma, and length) of the AIS in confocal image stacks (×63 magnification) were measured by manually identifying and precisely tracing along the region of colocalization between Ankyrin$_G$/Na$_v$1.6 and the green fluorescent signal of the native green fluorescent protein expressed within the axons of labeled RGCs using NIH ImageJ/Fiji package. Measurements of AIS length and distance were performed independently from calculations of cell size (dendritic field diameter, soma diameter, and soma volume) and retinal location. Measurements were reliable between three independent experimenters. In a few cases (<5), AISs were obscured, either because they overlapped with other AISs or because of interfering axon bundles, making it difficult to obtain an accurate measurement and to get agreement between examiners. In these cases, the AIS measurements were excluded from further analysis.

Simple three-dimensional tracing of dendritic architecture and Sholl analysis was performed in ImageJ/Fiji toolbox "Simple Neurite Tracer" (36). Full tracing, including compartment diameters of dendritic arbors, was performed in NeuronStudio (×20 magnification) (37). Tracing of the proximal axon was performed at higher magnification (×63).

Computational modeling
To analyze the response of model RGCs to intracellular current injections, we used the approach of compartment modeling (38). Thereby, current flow along the stimulated fiber and current flow across the neuronal membrane are simulated by a network of compartments with given electrical properties. We used membrane dynamics from Fohlmeister et al. (39) and slightly modified their sodium channel properties to better approximate the properties of Na$_v$1.6 channels. This was performed by shifting the activation curves to 6 mV more hyperpolarized; the potassium channel was modified accordingly. Ion channel densities for the five different

sections along the neuron (dendrites, soma, soma to AIS, AIS, and axon) can be found in table S1. The levels of voltage-gated sodium and potassium ion channels in the AIS were five times greater than those in the soma. Intracellular resistivity was set to 143.2 ohm·cm, specific membrane capacitance was set to 1 μF/cm^2, and model temperature was set to 33°C similar to experimental conditions.

To test the influence of realistic synaptic inputs (e.g., those measured in response to light stimuli) on membrane voltage, we used input currents elicited by a 400-μm spot onto the soma center of a ventral and dorsal OFF-α T RGCs, respectively; data were extracted from Warwick et al. [see figure 5 in (9) and Fig. 7E, inset]. In these simulations, all active ionic currents were blocked, essentially resulting in a passive membrane model.

The model was solved in MATLAB (MathWorks) using a custom written implicit (backward) Euler solver. Time step was set to 0.005 ms. The models of the traced cells ($n = 12$) used for simulations consisted of >1000 compartments; compartment length ranged from 1 μm (axon) to 5 μm (dendrite).

Statistical analysis
We measured linear correlation between two variables using Pearson's correlation coefficient. We used a two-sample t test, Welch's t test, or Wilcoxon rank sum test for comparison of two groups. Significance levels were set as follows: n.s., not significant, $P \geq 0.05$, $*P < 0.05$, $**P < 0.01$, and $***P < 0.001$. Numerical values are presented as means ± SEM except otherwise noted. Box plots use standard notation (first quartile, median, and third quartile). All statistical analysis except two-way repeated measures analysis of variance (ANOVA) (SPSS, IBM) was performed in MATLAB (MathWorks).

REFERENCES AND NOTES
1. T. Baden, P. Berens, K. Franke, M. Román Rosón, M. Bethge, T. Euler, The functional diversity of retinal ganglion cells in the mouse. *Nature* **529**, 345–350 (2016).
2. D. J. Margolis, A. J. Gartland, T. Euler, P. B. Detwiler, Dendritic calcium signaling in ON and OFF mouse retinal ganglion cells. *J. Neurosci.* **30**, 7127–7138 (2010).
3. V. Raghuram, P. Werginz, S. I. Fried, Scaling of the AIS and somatodendritic compartments in α S RGCs. *Front. Cell. Neurosci.* **13**, 436 (2019).
4. B. J. O'Brien, T. Isayama, R. Richardson, D. M. Berson, Intrinsic physiological properties of cat retinal ganglion cells. *J. Physiol.* **538**, 787–802 (2002).
5. D. J. Margolis, P. B. Detwiler, Different mechanisms generate maintained activity in ON and OFF retinal ganglion cells. *J. Neurosci.* **27**, 5994–6005 (2007).
6. K. J. Bender, L. O. Trussell, The physiology of the axon initial segment. *Annu. Rev. Neurosci.* **35**, 249–265 (2012).
7. H. Kuba, T. M. Ishii, H. Ohmori, Axonal site of spike initiation enhances auditory coincidence detection. *Nature* **444**, 1069–1072 (2006).
8. M. S. Hamada, S. Goethals, S. I. de Vries, R. Brette, M. H. P. Kole, Covariation of axon initial segment location and dendritic tree normalizes the somatic action potential. *Proc. Natl. Acad. Sci. U.S.A.* **113**, 14841–14846 (2016).
9. R. A. Warwick, N. Kaushansky, N. Sarid, A. Golan, M. Rivlin-Etzion, Inhomogeneous encoding of the visual field in the mouse retina. *Curr. Biol.* **28**, 655–665.e3 (2018).
10. B. Krieger, M. Qiao, D. L. Rousso, J. R. Sanes, M. Meister, Four alpha ganglion cell types in mouse retina: Function, structure, and molecular signatures. *PLOS ONE* **12**, e0180091 (2017).
11. P. L. Carras, P. A. Coleman, R. F. Miller, Site of action potential initiation in amphibian retinal ganglion cells. *J. Neurophysiol.* **67**, 292–304 (1992).
12. Z. F. Mainen, J. Joerges, J. R. Huguenard, T. J. Sejnowski, A model of spike initiation in neocortical pyramidal neurons. *Neuron* **15**, 1427–1439 (1995).
13. G. Stuart, J. Schiller, B. Sakmann, Action potential initiation and propagation in rat neocortical pyramidal neurons. *J. Physiol.* **505**, 617–632 (1997).

14. M. H. P. Kole, S. U. Ilschner, B. M. Kampa, S. R. Williams, P. C. Ruben, G. J. Stuart, Action potential generation requires a high sodium channel density in the axon initial segment. *Nat. Neurosci.* **11**, 178–186 (2008).

15. W. Hu, C. Tian, T. Li, M. Yang, H. Hou, Y. Shu, Distinct contributions of Na$_v$1.6 and Na$_v$1.2 in action potential initiation and backpropagation. *Nat. Neurosci.* **12**, 996–1002 (2009).

16. T. Boiko, A. Van Wart, J. H. Caldwell, S. R. Levinson, J. S. Trimmer, G. Matthews, Functional specialization of the axon initial segment by isoform-specific sodium channel targeting. *J. Neurosci.* **23**, 2306–2313 (2003).

17. A. Van Wart, J. S. Trimmer, G. Matthews, Polarized distribution of ion channels within microdomains of the axon initial segment. *J. Comp. Neurol.* **500**, 339–352 (2007).

18. E. Kordeli, S. Lambert, V. Bennett, Ankyrin$_G$. A new ankyrin gene with neural-specific isoforms localized at the axonal initial segment and node of Ranvier. *J. Biol. Chem.* **270**, 2352–2359 (1995).

19. D. Zhou, S. Lambert, P. L. Malen, S. Carpenter, L. M. Boland, V. Bennett, Ankyrin$_G$ is required for clustering of voltage-gated Na channels at axon initial segments and for normal action potential firing. *J. Cell Biol.* **143**, 1295–1304 (1998).

20. S. I. Fried, A. C. W. Lasker, N. J. Desai, D. K. Eddington, J. F. Rizzo III, Axonal sodium-channel bands shape the response to electric stimulation in retinal ganglion cells. *J. Neurophysiol.* **101**, 1972–1987 (2009).

21. I. M. Raman, B. P. Bean, Resurgent sodium current and action potential formation in dissociated cerebellar Purkinje neurons. *J. Neurosci.* **17**, 4517–4526 (1997).

22. Z. M. Khaliq, N. W. Gouwens, I. M. Raman, The contribution of resurgent sodium current to high-frequency firing in Purkinje neurons: An experimental and modeling study. *J. Neurosci.* **23**, 4899–4912 (2003).

23. A. Van Wart, G. Matthews, Impaired firing and cell-specific compensation in neurons lacking Na$_v$1.6 sodium channels. *J. Neurosci.* **26**, 7172–7180 (2006).

24. N. J. Hargus, A. Nigam, E. H. Bertram III, M. K. Patel, Evidence for a role of Na$_v$1.6 in facilitating increases in neuronal hyperexcitability during epileptogenesis. *J. Neurophysiol.* **110**, 1144–1157 (2013).

25. M. L. Risner, S. Pasini, M. L. Cooper, W. S. Lambert, D. J. Calkins, Axogenic mechanism enhances retinal ganglion cell excitability during early progression in glaucoma. *Proc. Natl. Acad. Sci. U.S.A.* **115**, E2393–E2402 (2018).

26. E. Lazarov, M. Dannemeyer, B. Feulner, J. Enderlein, M. J. Gutnick, F. Wolf, A. Neef, An axon initial segment is required for temporal precision in action potential encoding by neuronal populations. *Sci. Adv.* **4**, eaau8621 (2018).

27. M. H. P. Kole, First node of Ranvier facilitates high-frequency burst encoding. *Neuron* **71**, 671–682 (2011).

28. M. D. Evans, A. S. Dumitrescu, D. L. H. Kruijssen, S. E. Taylor, M. S. Grubb, Rapid modulation of axon initial segment length influences repetitive spike firing. *Cell Rep.* **13**, 1233–1245 (2015).

29. D. Bianchi, A. Marasco, A. Limongiello, C. Marchetti, H. Marie, B. Tirozzi, M. Migliore, On the mechanisms underlying the depolarization block in the spiking dynamics of CA1 pyramidal neurons. *J. Comput. Neurosci.* **33**, 207–225 (2012).

30. T. Kameneva, M. I. Maturana, A. E. Hadjinicolaou, S. L. Cloherty, M. R. Ibbotson, D. B. Grayden, A. N. Burkitt, H. Meffin, Retinal ganglion cells: Mechanisms underlying depolarization block and differential responses to high frequency electrical stimulation of ON and OFF cells. *J. Neural Eng.* **13**, 016017 (2016).

31. E. S. Milner, M. T. H. Do, A population representation of absolute light intensity in the mammalian retina. *Cell* **171**, 865–876.e16 (2017).

32. A. M. Rush, S. D. Dib-Hajj, S. G. Waxman, Electrophysiological properties of two axonal sodium channels, Na$_v$1.2 and Na$_v$1.6, expressed in mouse spinal sensory neurones. *J. Physiol.* **564**, 803–815 (2005).

33. A. H. Lewis, I. M. Raman, Resurgent current of voltage-gated Na$^+$ channels. *J. Physiol.* **592**, 4825–4838 (2014).

34. E. Neher, Correction for liquid junction potentials in patch clamp experiments. *Methods Enzymol.* **207**, 123–131 (1992).

35. J. Schindelin, I. Arganda-Carreras, E. Frise, V. Kaynig, M. Longair, T. Pietzsch, S. Preibisch, C. Rueden, S. Saalfeld, B. Schmid, J.-Y. Tinevez, D. J. White, V. Hartenstein, K. Eliceiri, P. Tomancak, A. Cardona, Fiji: An open-source platform for biological-image analysis. *Nat. Methods* **9**, 676–682 (2012).

36. M. H. Longair, D. A. Baker, J. D. Armstrong, Simple Neurite Tracer: Open source software for reconstruction, visualization and analysis of neuronal processes. *Bioinformatics* **27**, 2453–2454 (2011).

37. S. L. Wearne, A. Rodriguez, D. B. Ehlenberger, A. B. Rocher, S. C. Henderson, P. R. Hof, New techniques for imaging, digitization and analysis of three-dimensional neural morphology on multiple scales. *Neuroscience* **136**, 661–680 (2005).

38. W. Rall, in *Neural Theory and Modeling*, R. F. Reiss, Ed. (Stanford Univ. Press, 1964), pp. 73–97.

39. J. F. Fohlmeister, E. D. Cohen, E. A. Newman, Mechanisms and distribution of ion channels in retinal ganglion cells: Using temperature as an independent variable. *J. Neurophysiol.* **103**, 1357–1374 (2010).

Citation: P. Werginz, V. Raghuram, S. I. Fried, Tailoring of the axon initial segment shapes the conversion of synaptic inputs into spiking output in OFF-α T retinal ganglion cells. *Sci. Adv.* **6**, eabb6642 (2020).